Point spread function based image reconstruction in optical projection tomography

Trull, Anna; van der Horst, Jelle; Palenstijn, Willem Jan; van Vliet, Lucas; van Leeuwen, Tristan; Kalkman, Jeroen

DOI
10.1088/1361-6560/aa8945

Publication date
2017

Document Version
Accepted author manuscript

Published in
Physics in Medicine and Biology

Citation (APA)
Trull, A., van der Horst, J., Palenstijn, W. J., van Vliet, L., van Leeuwen, T., & Kalkman, J. (2017). Point spread function based image reconstruction in optical projection tomography. *Physics in Medicine and Biology*, *62*(19), 7784-7797. https://doi.org/10.1088/1361-6560/aa8945

Point spread function based image reconstruction in optical projection tomography

Anna K. Trull[1], Jelle van der Horst[1], Willem Jan Palenstijn[2], Lucas J. van Vliet[1], Tristan van Leeuwen[3], and Jeroen Kalkman[1]

[1]Department of Imaging Physics, Delft University of Technology, Lorentzweg 1, 2628 CJ Delft, The Netherlands
[2]Computational Imaging, Centrum Wiskunde & Informatica, Science Park 123, 1098 XG Amsterdam, The Netherlands
[3]Mathematical Institute, Utrecht University, Budapestlaan 6, 3584 CD Utrecht, The Netherlands

E-mail: a.k.trull@tudelft.nl

May 2017

Abstract. As a result of the shallow depth of focus of the optical imaging system, the use of standard filtered back projection in optical projection tomography causes space-variant tangential blurring that increases with the distance to the rotation axis. We present a novel optical tomographic image reconstruction technique that incorporates the point spread function (PSF) of the imaging lens in an iterative reconstruction. The technique is demonstrated using numerical simulations, tested on experimental optical projection tomography data of single fluorescent beads, and applied to high-resolution emission optical projection tomography imaging of an entire zebrafish larva. Compared to filtered back projection our results show greatly reduced radial and tangential blurring over the entire 5.2×5.2 mm^2 field of view, and a significantly improved signal to noise ratio.

Keywords: Image reconstruction techniques, Inverse problems, Tomographic image processing

1. Introduction

Optical tomographic imaging techniques such as optical diffraction tomography Wolf1969 and optical projection tomography (OPT) Sharp2002 are now among the standard imaging modalities for the study of cells, tissues and small animals. In OPT, light intensity projections of samples, such as zebrafish or (mouse) embryos, are measured in transmission or emission (fluorescence). From these projections, images are computed using tomographic reconstruction algorithms. OPT is used for in-vivo and ex-vivo imaging, whereby for ex-vivo imaging optical clearing techniques are used to

suppress light scattering.

In the quest for improved image resolution, high numerical aperture (NA) lenses are used to image the transmission or emission of the sample onto the detector. However, high NA lenses have a small depth of focus (DOF), which causes light that is emitted or absorbed outside of the focal region to be heavily blurred in the detector plane, thereby limiting the imaging depth. Moreover, standard reconstruction techniques, such as filtered back projection (FBP), are generally based on a straight ray approximation and ignore the diffraction of the light by the focusing lens. As a result, reconstructed OPT images can suffer from severe image degradation, leading to tangential blurring that increases with the distance to the rotation axis in the reconstructed image.

Hardware-based approaches to solve the depth of focus effect are either based on off-center focusing Chen2013 or scanning the focal plane through the sample Miao2010. Although, these techniques can reduce the depth of focus effect in the reconstructed image, they are complex to apply and increase the acquisition time.

A sinogram filtering using the frequency distance relationship (FDR) was developed by [XLE95], in which a space-variant inverse filter is applied to process the sinogram in Fourier space. The physical PSF of an optical imaging system was used as a filter in the FDR reconstruction of OPT data by [WSS07]. In this method the image is reconstructed, after filtering the sinogram, using standard FBP. A weighted FBP for quantitative fluorescence optical projection tomography was presented by [DMM$^+$08]. They used a space-variant weighting in the FBP reconstruction to correct for defocus related blur and isotropic emission of the fluorophores. However, this filter was only applied in one direction, which resulted in an increased radial full width at half maximum of the point spread function (PSF). To reduce the effect of the DOF both the radial and tangential direction, various processing methods were developed, which include the physical PSF in their approach. Deconvolution techniques with a space-variant PSF have been applied to the reconstructed image Nagy1997, Ott2011,Chen2012, Horst2016. However, the quality of this technique depends on the choice of many parameters of the applied reconstruction algorithm. Furthermore, deconvolution techniques have the disadvantage to amplify noise. To our knowledge, terahertz tomography is the only technique, where the beam shape is included in the reconstruction algorithm Recur2012. In this case an iterative approach was presented whereby the object is deconvolved with a Gaussian PSF and subsequently the straight ray inverse Radon transform was applied for reconstruction.

We present a PSF-based optical tomographic image reconstruction approach, in which the PSF of the focusing by the lens is directly included in the tomographic reconstruction instead of filtering the sinogram before, or the image after, reconstruction. First, a theoretical framework is provided that describes the PSF-based reconstruction. The application of the theory is demonstrated using numerical simulations of the tomographic imaging process. Second, our algorithm is tested under well-controlled experimental conditions. Finally, the technique is demonstrated on zebrafish larva imaging.

2. Image formation in optical projection tomography

In optical projection tomography (OPT), the goal is to determine the spatial distribution of absorption or emission strength of an object $f(x, y, z)$ from its projections. In emission OPT, the object is assumed to be homogeneously illuminated with light from the excitation source resulting in an excitation rate that is constant over the object f. A small fraction of the excitation light is absorbed and emitted isotropically. Hence, it is assumed that variations in local emission strength are caused by variations in fluorophore concentration only. The emitted radiation is imaged with an imaging system onto the detector, see Fig. 1(a).

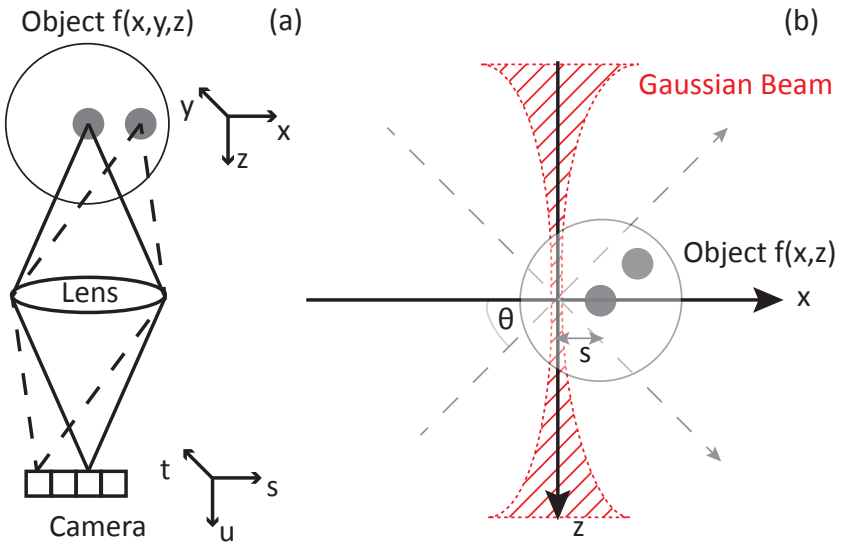

Figure 1. Schematic overview of the optical project tomography imaging system. (a) Optical imaging system consisting of a single lens making a projection of the object onto the camera. (b) OPT signal formation for diffractive optical beams (red dashed and hatched). The rotation angle is denoted by θ, the shift of the object s, and $f(x, z)$ is a slice of the object.

Following [Gu00], and assuming a single emitter at location x, y, z, in the object coordinate system, the intensity in the image space coordinate system is $I(s, t, u) = |h(x + Ms, y + Mt, z - M^2u)|^2$, with h^2 the incoherent PSF and M the magnification of the imaging system. Given the geometry in Fig. 1 (a) with the detector fixed at $u = 0$ and since the object can be considered as a sum of incoherent point sources, the measured intensity is a convolution of the object emission distribution with the PSF $|h(x, y, z)|^2$. For an imaging system with $M = -1$ and $u = 0$ the measured intensity on the detector is

$$I(s,t) = \iiint_{-\infty}^{\infty} f(x-s, y-t, z-u)|h(x,y,z)|^2 \,\mathrm{d}x\,\mathrm{d}y\,\mathrm{d}z|_{u=0}. \tag{1}$$

In the absence of diffraction, the PSF is $|h(x, y, z)|^2 = \delta(x, y)$. Under these

circumstances the convolution in Eq. 1 results in a line integral of the object $f(x, y, z)$, similar to the Radon transform at zero angle along the propagation direction Radon1917a. In OPT, diffraction causes the PSF to be non-ideal. The emitted light, originating along a straight path through the object, is (unsharply) imaged by a lens onto the detector. The shape of the 3D PSF can be calculated by Fourier optics, more in particular by Fresnel propagation of the emitted field through the lens onto the detector Goodman1996,Gu2000.

Following the derivation by van der Horst et al. Horst2016 we assume an integration on the detector in the t direction over the entire detector plane, which is a good approximation for objects that have optical properties that vary slowly along the y-axis. In this case the measured intensity in Eq. 1 becomes proportional to the convolution of the object with a 2-D cross-section of the 3-D PSF. Since the image of a point emitter by a lens results in a complex PSF, we describe it here through an analytical formula. In this way we can quantitatively validate our approach using simulations and compare our results with theory. We model the PSF $|h(x, z)|^2$ as a Gaussian-shaped beam of the wavelength λ and in focus beam waist w_0 Siegman1986 as

$$|h(x,z)|^2 = \frac{1}{\sqrt{1+\left(\frac{z}{z_R}\right)^2}} \exp\left(-\frac{x^2}{w_0\sqrt{1+\left(\frac{z}{z_R}\right)^2}}\right), \tag{2}$$

where $z_R = \pi w_0^2/\lambda$ is the Rayleigh range (half the depth of focus). The numerical aperture is given by NA $= w_0/z_R$ in Eq. 1. The two-dimensional convolution of the PSF over the object is indicated in Fig. 1(b).

In tomographic imaging, we obtain the projections of the emission as a function of the lateral shift s and the rotation angle θ of the object. From Eq. 1, it can be derived that the measured projection at the angle θ and shift s is

$$p(s,\theta) = \iint_{-\infty}^{\infty} f[(x-s)\cos\theta + z\sin\theta, (x-s)\cos\theta - z\sin\theta]\ |h(x,z)|^2\,\mathrm{d}x\,\mathrm{d}z\,, \tag{3}$$

with the angle $\theta \in [0, 2\pi]$. The projections $p(s, \theta)$ are commonly visualized in a sinogram, where the convolution in Eq. 3 describes the blurring in the sinogram due to the tomographic imaging system.

The projection data $p(s, \theta)$ is not measured in a continuous way, as defined by Eq. 3, but is sampled at discrete lateral positions for a finite set of angles. Hence, the inverse solution cannot be determined analytically, but only through a search for the function $f(x, z)$ that optimizes an objective function. The projection of Eq. 3, $p(s, \theta)$, is limited to a finite integration area D given by $D \in [-l/2, l/2]$ for offsets $s \in [-l/2, l/2]$ and l is the size of the field of view. The projection is then represented by a matrix multiplication with the object f discretized by sampling $f(x, z)$ on a regular cell-centered grid, within the square object domain D^2 at locations x_i, z_j, with $i = 1, 2, \ldots, n$, $j = 1, 2, \ldots, n$ where n is the number of pixels in each direction of the object and equal to the number of lateral pixels in the projection. This leads to an image matrix of $f(x_i, z_i) \in \mathbb{R}^{n\times n}$,

which is stacked in a vector $\mathbf{f} \in \mathbb{R}^{n^2}$. The convolution of Eq. 3 is discretized into a geometry matrix $\mathbf{A} \in \mathbb{R}^{m \cdot n, n^2}$, with m the number of projection angles. A row of the matrix $\mathbf{A}$ represents a the Gaussian PSF at lateral distance s_i and angle θ_k. The matrix elements of $\mathbf{A}$ are

$$a_{(k-1)n+i,:} = |h[(x_i - s_i)\cos\theta_k + z_i \sin\theta_k, (x_i - s_i)\cos\theta_k - z_i \sin\theta_k]|^2. \quad (4)$$

In this way, a shifted and rotated PSF is represented in a single row of the $\mathbf{A}$ matrix. First, all shifts for one angle are addressed, which is subsequently repeated for all angles. The acquisition domain of the measured projections are the set of samples (s_i, θ_k), with $k = 1, 2, \ldots, m$. The discrete projections $p(s_i, \theta_k) \in \mathbb{R}^{n,m}$ are stacked into a vector $\mathbf{p} \in \mathbb{R}^{n \cdot m, 1}$.

After discretization, the object, $\mathbf{f}$, can be reconstructed by finding a solution to the optimization problem

$$\underset{\mathbf{f}}{\text{argmin}} \quad \frac{1}{2}\|\mathbf{A} \cdot \mathbf{f} - \mathbf{p}\|_2^2, \quad (5)$$

where $||\cdot||_2$ denotes the Euclidean norm. Equation 5 can be solved using a least squares optimization method based on conjugate gradients.

3. Image reconstruction

Tomographic reconstructions are performed on a computer with Intel(R) Xeon(R) CPU Processor (E5-1620 v3@3.50 GHz), 32 GB installed memory and a 64-bit operating system. The data are processed using software written in the commercial software package MATLAB (Mathworks, R2016a). Simulated sinograms are constructed using the discretized version of Eq. 3 for an initial object f. Following the data processing flow chart in Fig. 2, an initial guess of the image is created by filtered back projection (FBP) (input reconstruction). An improved estimate for the object is made by least-squares optimization of Eq. 5 using the MATLAB function *lsqr* Paige1982, Barrett1994, which uses a conjugate-gradient type iterative algorithm on the normal equations. It takes as input the projection data, the initial guess of the image (created by FBP), the maximum number of iterations to perform, the absolute tolerance, and the projection matrix $\mathbf{A}$. The absolute tolerance of the method is chosen to be 10^{-6}.

Explicitly computing and storing the projection matrix $\mathbf{A}$ for a realistic image size of 1000 by 1000 would cost around 8 terabytes of memory, which is infeasible. Instead of requiring a precomputed version of $\mathbf{A}$, the MATLAB function *lsqr* also allows providing a routine that evaluates multiplication by $\mathbf{A}$ and its transpose for every angle individually. Here, multiplication by $\mathbf{A}$ corresponds to (PSF-based) forward projection of an input image, and multiplication by the transpose of $\mathbf{A}$ corresponds to (PSF-based) back projection of an input sinogram. We list the pseudo-code for calculating the forward and backward projection in Algorithm 1. It uses the built-in MATLAB function *imrotate* with bilinear interpolation to obtain the object at different angles. For every individual angle, the PSF is translated laterally over the sample, so the forward model

of the projection has the structure of a one-dimensional convolution in the translation direction, followed by a sum in the direction orthogonal to that. We implement this by a multiplication of the Fourier transform of the object and the Fourier transform of the PSF for every column, followed by a sum for every row. To perform these operation correctly we zero-pad the sinogram to twice its size in the scanning direction. The back projection operator performs the adjoint/transpose variants of these steps in reverse order.

We set the maximum number of *lsqr* iterations to different hand-picked numbers depending on the convergence of the algorithm, which depends on the data that is to be reconstructed. In the current implementation one iteration of the *lsqr* algorithm, for one slice of 1000 by 1000 pixels, takes approximately two minutes.

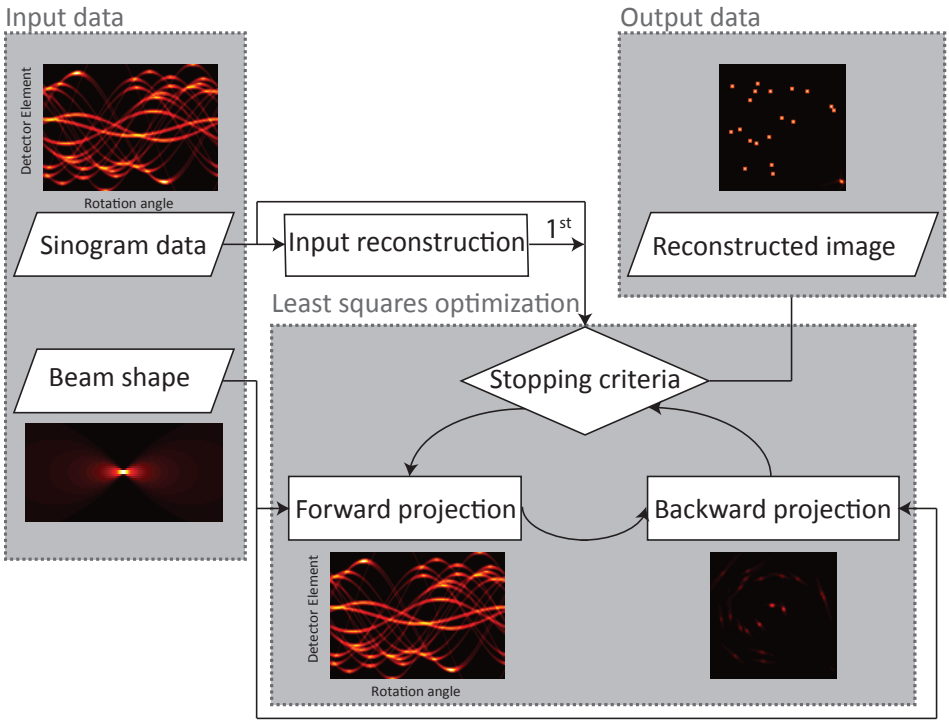

Figure 2. Schematic illustration of the data analysis algorithm for the PSF-based reconstruction. The input reconstruction is only used in the first iteration.

To enable a qualitative comparison of the reconstructed images, the FBP reconstruction is scaled in the following way. The reconstructed FBP image is forward projected to obtain its sinogram. The scaling factor α_{opt} is then given by

$$\alpha_{\text{opt}} = \underset{\alpha}{\text{argmin}} \quad \|\alpha \mathbf{A}\mathbf{f}_1 - \mathbf{A}\mathbf{f}_2\|_2^2, \tag{6}$$

where $\mathbf{f_1}$ is the FBP reconstructed image and $\mathbf{f_2}$ the PSF-based reconstructed image. The scaling factor α_{opt} is then given in closed-form by

$$\alpha_{\text{opt}} = \frac{(\mathbf{A}\mathbf{f}_1)^{\text{T}}(\mathbf{A}\mathbf{f}_2)}{||\mathbf{A}\mathbf{f}_1||_2^2}. \tag{7}$$

Subsequently, the FBP reconstruction is scaled with α_{opt} to obtain an image intensity distribution in the reconstruction that corresponds to equal projection data. ‡

Algorithm 1 Calculate $\mathbf{p} = \mathbf{A}\mathbf{f}$ or $\mathbf{f} = \mathbf{A}^{\mathrm{T}}\mathbf{p}$

Require: $\mathbf{f}$, *mode*, beam parameters

Notation: Denote by (I)$\mathrm{FT_C}$ taking an (inverse) 1D Fourier transform of every column of an image, by (I)$\mathrm{FT_1}$ taking the (inverse) 1D Fourier transform, by $\mathrm{Sum_R}$ taking the sum of every row of an image, and by $\mathbf{p}^i$ the i-th row of a sinogram $\mathbf{p}$.
Pre-compute the 2D beam shape of a horizontal beam and $\mathrm{FT_C}$(Beam)
if mode = 'not transposed', **then** ▷ Forward operator, $\mathbf{p} = \mathbf{A}\mathbf{f}$
    for $i = 1 : \mathrm{angle_{count}}$ **do**
        $\mathbf{f}_r = \mathbf{f}$ rotated by the current angle
        $\mathbf{p}^i = \mathrm{IFT_1}(\mathrm{Sum_R}(\mathrm{FT_C}(\mathbf{f_r}) \cdot \mathrm{FT_C}(\mathrm{Beam})))$
else ▷ Backward operator, $\mathbf{f} = \mathbf{A}^{\mathrm{T}}\mathbf{p}$
    $\mathbf{f}$ = the zero image
    for $i = 1 : \mathrm{angle_{count}}$ **do**
        $\mathbf{t}$ = Multiply each column of $\mathrm{FT_C}$(Beam) by $\mathrm{FT_1}(\mathbf{p}^i)$
        $\mathbf{u} = \mathrm{IFT_C}(t)$ rotated by the reverse angle
        $\mathbf{f} = \mathbf{f} + \mathbf{u}$
return $\mathbf{p}$ or $\mathbf{f}$

4. Results

4.1. OPT Simulations

The original object for the simulation is given in Fig. 3 (a). The object, with a size of 15×15 mm^2 (100×100 pixels), consists of isolated point sources, with a peak emission strength of 100 in the center pixel of the source and an emission strength set to 50 for the eight pixels around the center of the source. The object is blurred by convolving it with a Gaussian PSF for an emission wavelength of 514 nm with a waist $w_0 = 10$ µm, DOF= 1.2 mm, NA= 0.016, see Fig. 3 (b). Figure 3 (c) shows the same simulation for $w_0 = 100$ µm, DOF=122 mm, NA= 0.0016. The object data is processed following the flowchart in Fig. 2. The maximum number of iterations is set to 200.

The reconstruction results using filtered back projection (MATLAB function *iradon*) and the proposed method are depicted in Fig. 3. Figure 3 (d) and (e) show the FBP reconstructed images, which is based on straight parallel rays, for the two Gaussian PSFs. In Fig. 3 (d) it is clearly visible that, compared to the original object, the emission contrast is much lower due to the small DOF. Moreover, the reconstructed image shows that the emitters are strongly blurred in the tangential direction due to the strong divergence of the Gaussian PSF, as shown in Fig. 3(b). The tangential

‡ Our code to perform these calculations can be made available on request.

resolution deteriorates with increasing distance to the center of rotation whereas the radial resolution is slightly deteriorated, but does not depend on the distance from the center of rotation. The insets show this in more detail for two emitters. For a PSF with a larger beam waist, modeling a low NA, large DOF, imaging system, Fig. 3 (e) shows that there is some blurring in the reconstructed image. However, for this larger beam waist this effect depend very weakly on the distance to the center of rotation since the Gaussian PSF has much lower divergence, as shown in Fig. 3(c). Figure 3 (f) and (g) show our PSF-based reconstruction. In Fig. 3 (f) the contrast is completely restored, the strong tangential blurring is absent, and the reconstructed image is identical to the input image. Figure 3 (g) shows that also for a larger beam waist, the blurring of the emitter is fully corrected for by our PSF-based reconstruction method.

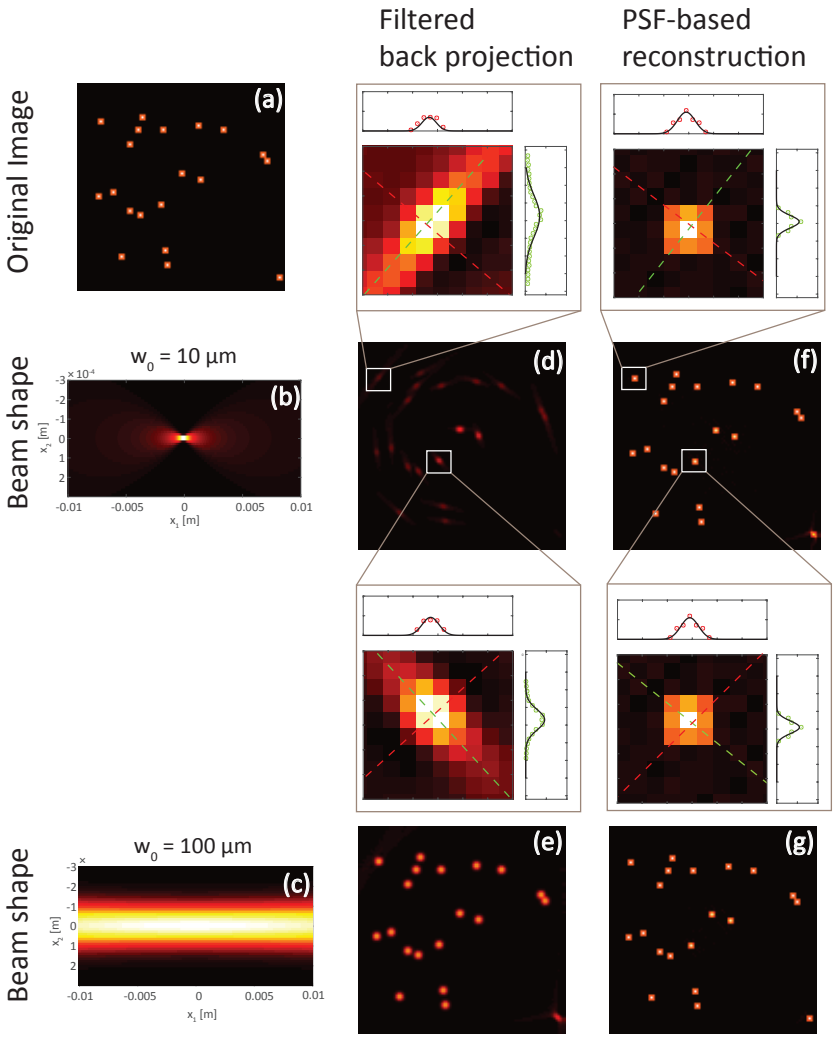

Figure 3. Simulation of the FBP and PSF-based image reconstruction. (a) Input image, (b) Gaussian PSF for $w_0 = 10$ µm. (c) Gaussian PSF for $w_0 = 100$ µm. (d, e) Reconstruction using FBP for the two Gaussian PSFs. (f, g) Reconstruction using the PSF-based approach for the two Gaussian PSFs.

4.2. Fluorescent bead OPT imaging

The PSF-based reconstruction method is tested with experimental OPT imaging of a sample with fluorescent bead emitters embedded in an agarose emulsion. The experimental set-up is described in more detail in Horst2016, the main parameters of importance are briefly discussed. The experimentally determined Gaussian PSF has a beam waist in focus of $w_0 = 6$ µm with the measured beam shape used in the PSF-based reconstruction. Emission from the center of the object is focused onto the camera plane by the imaging lens. The field of view of the experimental data is 5.2×5.2 mm^2. In the lateral direction, the detector has 1344 pixels per projection and 360 projections are acquired over 360 degrees with a one degree spacing. The total dataset consist of 1024 sinograms covering a length of 4 mm along the rotation axis .

The measured data is pre-processed as follows. First, photo bleaching is corrected with a characteristic e^{-1} timescale of 798 seconds. Second, a constant background emission is removed from the sinogram. Third, the center of mass for each projection is estimated from the ratio of the integral of the projection times its transverse coordinate to the integral of the projection. Fourth, the center of rotation is determined from the centers of mass for all acquisition angles. Fifth, the center of rotation of the object is aligned with the center of the detector rows by shifting the data along the lateral dimensionAzevedo1990. Subsequently, the 1024 sinograms are combined into 32 averaged sinograms. The averaged sinograms are further pre-processed. The noise is reduced by applying a non-local means de-noising algorithm as described by Buades et al. Buades2004. The half size for the de-noising window is chosen to be 9 pixels. The width of the Gaussian filter relative to its maximum intensity is set to 0.5, the search width is set to 10 pixels and the limited number of dimensions for the principal component analysis is 20. Prior to the reconstruction, the sinograms are scaled to achieve a quantitative comparison of the image quality of the two methods. Subsequently, PSF-based reconstruction of the data is performed over 4000 iterations.

Figure 4(a) shows the reconstruction of an averaged sinogram of the experimental data using FBP. Similar to the simulations, the single point emitters appear blurred in the FBP reconstruction. In Fig. 4 (b) this is more clearly demonstrated by the zoom-in on the individual beads and the normalized cross-sections of the emitters. The cross sections show that the emission profiles in the reconstruction are broad and have a Gaussian-shape. Figure 4 (c) shows the same emitters, but reconstructed with our PSF-based approach. The emitters are brighter in comparison to the background and an improvement of the resolution is visible compared to the reconstruction using FBP. The quality of the reconstruction is analyzed by estimating the full width at half maximum (FWHM) of the Gaussian function fitted to each peak and is summarized Table 1. Our PSF-based reconstruction shows a significant reduction of the FWHM in both axial and tangential direction.

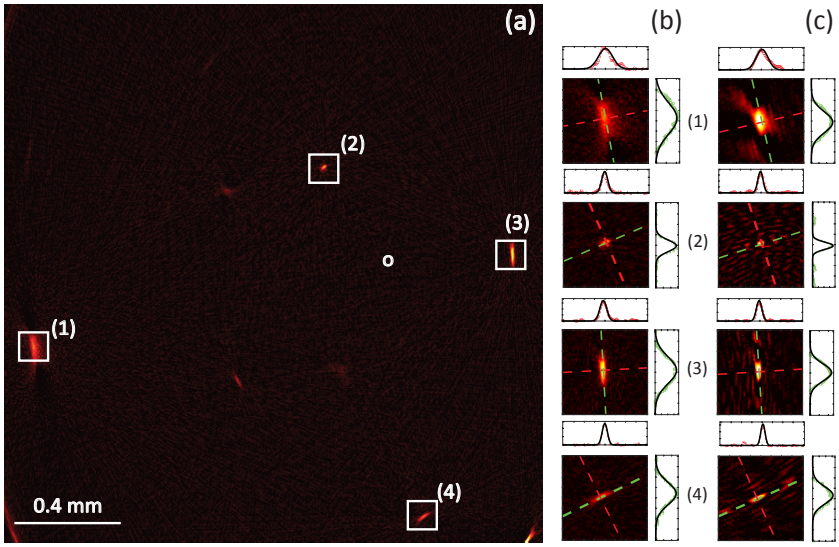

Figure 4. Comparison of the FBP and PSF-based reconstruction for a single averaged sinogram. (a) FBP image reconstruction of fluorescent bead data. The circle denotes the center of rotation. (b) Zoom in on reconstructed points of (a). (c) PSF-based reconstruction of the same points as in (b).

Table 1. FWHM resolution (µm) in axial and tangential direction for the FBP and the PSF-based reconstruction for four fluorescent beads. Each row corresponds to the beads indicated in Fig. 4. The errors indicate 95 % confidence intervals.

Method	FBP		PSF-based	
Bead #	Radial FWHM	Tangential FWHM	Radial FWHM	Tangential FWHM
1	22.3 ± 0.6	50.1 ± 1.3	16.2 ± 0.6	30.0 ± 1.0
2	9.6 ± 0.3	18.0 ± 0.5	7.1 ± 0.3	10.0 ± 0.4
3	10.7 ± 0.13	42.1 ± 0.6	8.3 ± 0.2	24.9 ± 0.5
4	8.3 ± 0.2	34.9 ± 0.9	6.3 ± 0.2	24.0 ± 0.6

4.3. Zebrafish larva OPT imaging

The proposed PSF-based reconstruction is applied to an OPT scan of a 10 days old transgenic zebrafish larva to illustrate the performance on biological samples. The zebrafish cellular membranes are labeled with green fluorescent protein. The zebrafish larva is euthanized in ice water at the Erasmus Medical Center, Rotterdam according to animal welfare regulations. Animal experiments are approved by the Animal Experimentation Committee of the Erasmus MC, Rotterdam.

The zebrafish is mounted in agarose in our OPT system. The same experimental parameters are used as for the fluorescent bead data, but for the zebrafish imaging a total of 1791 sinograms are acquired covering a distance of 6.9 mm along the rotation axis. For all 1791 slices, the tomographic image is reconstructed using FBP and the PSF-based approach (no slice averaging). Prior to the reconstruction, the sinograms are scaled to achieve a better quantitative comparison of the two methods. The number of iterations

for every reconstruction is set to two for which good convergence of the reconstruction is observed. The reconstruction of the zebrafish larva is depicted in Fig. 5. Figure 5(a) shows the reconstruction of a single transverse slice of the data using FBP. Although the zebrafish structure is visible, the reconstruction is corrupted by radial streak artifacts, shows significant blurring, and has limited image contrast. Figure 5 (b) shows our PSF-based reconstruction of the same transverse slice. Figure 5 (c) shows the anatomy of an optical cleared zebrafish larva, of similar age, in transverse view obtained from transmission OPT from the Zebrafish Anatomy Portal Zebrafish2016 and is used for anatomical reference. The quality of the reconstructed image is significantly improved in terms of contrast, artifact removal, and resolution. Figures 5 (d,e) show two cross sections through the data that illustrate the large improvement in image contrast and resolution. In our PSF-based reconstructed image the major anatomical parts are much better resolved compared to the reconstruction using FBP (see Fig. 5 (a) and (b)). Similar effects are visible in Figure 6, which shows a coronal cross-section through the same data. Figure 6 (a) and (b) show the reconstruction using FBP and the PSF-based reconstruction. Figure 6 (c) shows a transmission OPT image of the anatomy of a 7-13 days old, optically cleared, zebrafish larva in coronal view Zebrafish2016. An even better view on the obtained image improvement achieved by our PSF-based reconstruction can be seen in a video (Visualization 1), which shows a side by side comparison of transverse, coronal, and sagittal planes of the zebrafish using both reconstruction techniques.

5. Discussion and conclusion

We present a reconstruction algorithm routine, where the physical PSF is included in the reconstruction. Our PSF-based image reconstruction approach shows a significant improvement in OPT image quality compared to standard FBP reconstruction. In contrast to other approaches, our method incorporates the imaging geometry in the tomographic image reconstruction. As such we do not rely on filtering or deconvolution methods applied in the sinogram or image domain. A quantitative comparison of the quality of our image reconstruction algorithm with other state-of-the-art image reconstruction techniques is currently in progress Trull2017b. The presented reconstruction method employs a 2-D reconstruction, processing the data volume slice by slice. Despite this simplification, excellent image quality is obtained. We attribute this to the fact that the zebrafish has structures that, in general, vary slowly along the length of the zebrafish. In principle our PSF-based approach could be extended to three dimensions, however, this would significantly increase the memory requirements of the routine that performs the multiplication with the system matrix and its transpose, as well as the computation time. For the full image size of 1344 by 1024 pixels, this 3D implementation is currently not feasible.

The reconstruction time for one slice using the PSF-based algorithm is currently about two minutes for one iteration. This potentially can be reduced by converting the presented algorithm from MATLAB to another programming language, such as C++,

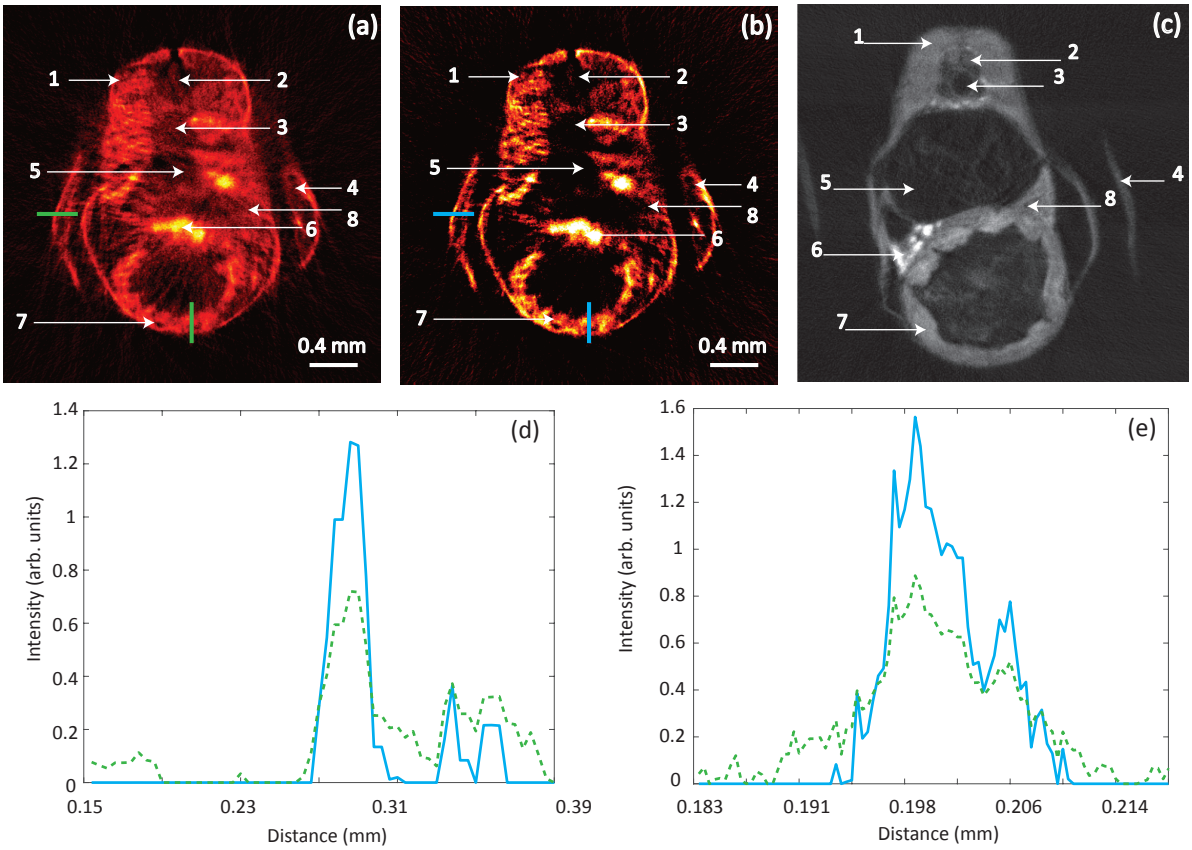

Figure 5. Transversal slice through the OPT reconstruction of a zebrafish larva. (a) FBP reconstruction with anatomical structures indicated. (b) PSF-based reconstruction.(c) Anatomy of a 7-13 days old optical cleared zebrafish larva Zebrafish2016, with anatomical features: (1) myotome, (2) spinal cord, (3) precaudal vertebra, (4) pectoral fin, (5) anterior chamber swim bladder, (6) pancreas, (7) intestinal bulb and (8) liver. (d) Cross-section in horizontal direction at line indicated in (a, b). (e) Cross-section in vertical direction at line indicated in (a, b). In (d, e) the green dashed line indicates the FBP and the blue solid line indicates the PSF-based approach.

or using a GPU. Moreover, for a slice-based reconstruction of three-dimensional objects, the reconstruction of different slices can be parallelized. A speed-up by a factor of 200 has been observed by Leeser et al. for parallel slice processing Leeser2014. Finally, since the PSF is varying slowly over many of the grid-points, relatively few grid points sample the beam at its narrow waist in the focal area. Hence, by representing the reconstruction problem in a different set of basis functions, potentially the size of the reconstruction problem can be reduced while obtaining the same reconstruction result.

In the reconstructions we observed that the convergence of the algorithm is strongly related to the noise level in the projections. The presented fluorophore bead data had an SNR, averaged over all the sinograms, of 31 ± 3 dB, whereas the zebrafish data had an average SNR of 67 ± 10 dB. Moreover, the zebrafish data is non-sparse compared to the bead data, which promotes convergence. As a result, the reconstruction of the

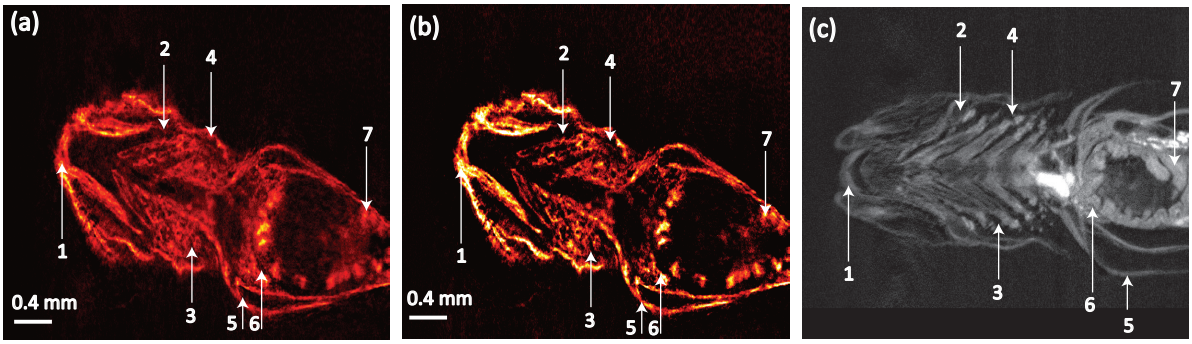

Figure 6. Coronal slice through the OPT reconstruction of a zebrafish larva (excluding the tail). (a) FBP reconstruction with anatomical structures indicated. (b) PSF-based reconstruction. (c) Anatomy of a 7-13 days old optical cleared zebrafish larva Zebrafish2016, with anatomical features: (1) intermandibularis, (2) ceratohyal, (3) opercular cavity, (4) opercle, (5) pectorial fin, (6) liver and (7) intestinal bulb.

fluorophore beads needed 4000 iterations, whereas the reconstruction of the zebrafish needed only 2 iterations to convergence.

In its current implementation, the PSF-based reconstruction is without including any prior information or regularization. Improvement of the convergence of the optimization possibly can be achieved by masking the data or by applying regularization methods. For example, for the sparse bead sample reconstruction, sparsity promoting ℓ_1 norm regularization, can aid in the reconstruction accuracy as well as in the convergence rate as was shown by [KKL$^+$07].

The proposed reconstruction technique can be extended to even higher NAs, potentially further improving the image resolution. Besides the significantly improved image quality, our PSF-based reconstruction has the advantage that arbitrary beam shapes can be incorporated in the reconstruction. In addition, other physical processes, such as refraction or scattering, can be included in the PSF-based reconstruction. The presented PSF-based reconstruction is useful in other fields of optical tomographic imaging where beam propagation deviates from the ideal straight ray such as in optical diffraction tomography, transmission OPT, electron tomography, terahertz tomography, and (phase-contrast) X-ray tomography.

Acknowledgments

The authors would like to thank Dr Robert Bryson-Richardson of the School of Biological Sciences, Monash University, Australia for the use of the transmission OPT images. This research is supported by the Dutch Technology Foundation STW, which is part of the Netherlands Organization for Scientific Research (NWO), and which is partly funded by the Ministry of Economic Affairs.

[ASFM90] Stephen G. Azevedo, Daniel F. Schneberk, J. Patrick Fitch, and Harry E. Martz. Calculation of the rotational centers in computed tomography sinogram. *IEEE Trans. Nucl. Sci.*, 37(4):1525–1540, 1990.

[BBC+94] R. Barrett, M. Berry, T. F. Chan, J. Demmel, J. Donato, J. Dongarra, V. Eijkhout, R. Pozo, C. Romine, and H. Van der Vors. Templates for the solution of linear systems: Building blocks for iterative methods. *SIAM*, 1994.

[BCM04] Antoni Buades, Bartomeu Coll, and Jean Michel Morel. On image denoising methods. Technical report, Technical Note, CMLA (Centre de Mathematiques et de Leurs Applications), 2004.

[CAK+13] L. Chen, N. Andrews, S. Kumar, P. Frankel, J. McGinty, and P. M. French. Simultaneous angular multiplexing optical projection tomography at shifted focal planes. *Opt. Lett.*, pages 851–853, 2013.

[CMT+12] Lingling Chen, James McGinty, Harriet B. Taylor, Laurence Bugeon, Jonathan R. Lamb, Margaret J. Dallman, and Paul M. W. French. Incorporation of an experimentally determined MTF for spatial frequency filtering and deconvolution during optical projection tomography reconstruction. *Opt. Express*, 20(7):7323–7337, Mar 2012.

[DMM+08] A Darrell, H Meyer, K Marias, M Brady, and J Ripoll. Weighted filtered backprojection for quantitative fluorescence optical projection tomography. *Phys. Med. Biol.*, 53:38633881, 2008.

[Goo96] J.W. Goodmann. *Introduction to Fourier Optics*. MaGraw-Hill, 2nd edition, 1996.

[Gu00] Min Gu. *Advanced Optical Imaging Theory*. Springer, 2000.

[KKL+07] S.-J. Kim, K. Koh, M. Lustig, S. Boyd, and D. Gorinevsky. An interior-point method for large-scale l_1-regularized least squares. *IEEE J. Sel. Topics Signal Process*, pages 606 – 617, 2007.

[LMB14] M. Leeser, S. Mukherjee, and J. Brock. Fast reconstruction of 3D volumes from 2D CT projection data with GPUs. *BMC Research Notes*, 2014.

[MHM+10] Q. Miao, J. Hayenga, M. G. Meyer, T. Neumann, A. C. Nelson, and E. J. Seibel. Resolution improvement in optical projection tomography by the focal scanning method. *Opt. Lett.*, 35:3363–3365, 2010.

[NO97] James G. Nagy and Dianne P. O'Leary. Fast iterative image restoration with a spatially-varying PSF. *Proc. SPIE 3162, Advanced Signal Processing: Algorithms, Architectures, and Implementations VII*, page 884, 1997.

[PS82] C. C. Paige and M. A. Saunders. LSQR: An algorithm for sparse linear equations and sparse least squares. *ACM*, 1982.

[RGMH+12] B. Recur, J. P. Guillet, I. Manek-Hönninger, J. C. Delagnes, W. Benharbone, P. Desbarats, J. P. Domenger, L. Canioni, and P. Mounaix. Propagation beam consideration for 3D THz computed tomography. *Opt. Express*, 20(6):5817 – 5829, 2012.

[RP86] Johann Radon and P.C. Parks. On the determination of functions from their integral values along certain manifolds. *IEEE Trans. Med. Imaging*, 4:170176, 1986. Translation of the original paper by Johann Radon 1917.

[SAP+02] J. Sharpe, U. Ahlgren, P. Perry, B. Hill, A. Ross, J. Hecksher-Sørensen, R. Baldock, and D. Davidson. Optical projection tomography as a tool for 3D microscopy and gene expression studies. *Science*, pages 541–545, 2002.

[Sie86] Anthony E. Siegman. *Lasers*. University Science Books, 1986.

[SMCBR12] David Salgadob, Christophe Marcelleb, Peter D. Currieb, and Robert J. Bryson-Richardson. The zebrafish anatomy portal a novel integrated resource to facilitate zebrafish research. *Developmental Biology*, 372(372):1–4, 2012.

[TORN+11] M. Temerinac-Ott, O. Ronneberger, R. Nitschke, W. Driever, and H. Burkhardt. Spatially variant Lucy Richardson deconvolution for multiview fusion of microscopal 3D images. *IEEE International Symposium on Biomedical Imaging: From Nano to Macro*, pages 899 – 904, 2011.

[Tru17] A.K. Trull. Comparison of image reconstruction techniques in optical projection tomography. *Manuscript in preparation*, 2017.

[vdHK16] Jelle van der Horst and Jeroen Kalkman. Image resolution and deconvolution in optical tomography. *Opt. Express*, 24(21):24460–24472, Oct 2016.

[Wol69] E. Wolf. Three-dimensional structure determination of semi-transparent objects from holographic data. *Optics Communications*, pages 153 – 156, 1969.

[WSS07] Johnathon R Walls, John G. Sled, and James Sharp. Resolution improvement in emission optical projection tomography. *Phys Med Biol.*, 52(10):2775–90., 2007.

[XLE95] W. Xia, R. M. Lewitt, and P. R. Edholm. Fourier correction for spatially variant collimator blurring in SPECT. *IEEE Trans. Med. Imaging*, 14(14):100–115, 1995.